Time-resolved operando studies of carbon supported Pd nanoparticles under hydrogenation reactions by X-ray diffraction and absorption

This is a pre print version of the following article:

Original Citation:

Availability:

This version is available http://hdl.handle.net/2318/1728871 since 2020-02-19T16:58:15Z

Published version:

DOI:10.1039/c7fd00211d

Terms of use:

(Article begins on next page)

16 July 2024

Time-resolved operando studies of carbon supported Pd nanoparticles under hydrogenation reactions by X-ray diffraction and absorption

Aram L. Bugaev,[a,b,*] Oleg A. Usoltsev,[a] Andrea Lazzarini,[c] Kirill A. Lomachenko,[d] Alexander A. Guda,[a] Riccardo Pellegrini,[e] Michele Carosso,[b] Jenny G. Vitillo,[b,f] Elena Groppo,[b] Jeroen A. van Bokhoven,[g,h] Alexander V. Soldatov,[a] Carlo Lamberti[a,i,*]

[a] The Smart Materials Research Center, Southern Federal University, Zorge Street 5, 344090, Rostov-on-Don, Russia
[b] Department of Chemistry, NIS Interdepartmental Centre and INSTM Reference Centre, University of Turin, via Quarello 15A, 10135 Turin, Italy
[c] Centre for Materials Science and Nanotechnology, Department of Chemistry, University of Oslo, Sem Saelands vei 26, 0315 Oslo, Norway
[d] European Synchrotron Radiation Facility (ESRF), 71 avenue des Martyrs, CS 40220, 38043 Grenoble Cedex 9, France
[e] Chimet SpA-Catalyst Division, via Di Pescaiola 74, Arezzo, Italy
[f] Department of Chemistry, University of Minnesota, 207 Pleasant Street S.E., Minneapolis, Minnesota 55455-0431, United States
[g] Institute for Chemical and Bioengineering, ETH Zurich, Vladimir-Prelog-Weg 1, 8093 Zurich, Switzerland
[h] Laboratory for Catalysis and Sustainable Chemistry, Paul Scherrer Institute, 5232 Villigen, Switzerland
[i] Department of Physics and CrisDi Interdepartmental Centre, University of Turin, via Pietro Giuria 1, 10125 Turin, Italy

*Corresponding authors: arambugaev@gmail.com ; carlo.lamberti@unito.it

Formation of palladium hydride and carbide phases in palladium-based catalysts is a critical process which change the catalytic performance and selectivity of the catalysts in important industrial reactions, such as selective hydrogenation of alkynes or alkenes. We present a comprehensive study of the palladium nanoparticles (NPs) under various external conditions by *in situ* and *operando* X-ray absorption spectroscopy and diffraction, to characterize palladium hydride and carbide phases, and their distribution over the volume of the NPs. We demonstrate how the simultaneous analysis of extended X-ray absorption fine structure spectra (EXAFS) and X-ray powder diffraction (XRPD) allows discriminating between the inner "core" and outer "shell" regions of the nanoparticle in case of hydride phase formation at different temperatures and under different hydrogen pressures, indicating that the amount of hydrogen in the shell region of the nanoparticle is lower than that in the core. In the case of palladium carbide, advanced analysis of X-ray absorption near-edge structure (XANES) spectra allows detecting carbon-containing molecules adsorbed at surface of the nanoparticles. In addition, H/Pd and C/Pd stoichiometries of PdH_x and PdC_y phases were obtained by theoretical modelling and fitting of XANES spectra. Finally, the collection of *operando* XRPD patterns allowed us to highlight during ethylene hydrogenation reaction periodic oscillations of non-regular shape of the NPs core lattice parameter, that resulted to be in phase with the MS signal of the C_2H_6 product and in antiphase with the MS signal of the H_2, highlighting an interesting direct structural-reactivity relationship. The presented studies are hereby showing how combination of X-ray absorption and diffraction can highlight the structure of core, shell and surface of the palladium nanoparticles and prove their relevant role in catalysis.

1. Introduction

Palladium-based materials, in particular nanoparticles (NPs), find numerous applications in industry, such as catalysts for selective hydrogenation reactions. Palladium is the metal of choice for semi-hydrogenation of alkadienes and alkynes in mixtures of alkyne/alkene and alkadiene/alkene respectively.[1-4] Palladium is prone to formation of carbides and hydrides and therefore, under reaction conditions, exposure of the catalyst to a mixture of H_2 and hydrocarbons may lead to formation of palladium hydride[5-13] or carbide[5, 12, 14, 15] phases, that may dramatically affect the catalytic activity and selectivity.[4, 14] For catalytic applications, it is important to understand the role of surface, subsurface and bulk hydrogen and carbon atoms[14] and the molecular-level picture of the catalytic hydrogenation over palladium nanoparticles, which are both still under debate.[4, 14-18]

Formation of both palladium hydride and carbide phases increases the lattice parameter which can be effectively detected by X-ray powder diffraction (XRPD).[12, 19, 20] This technique provides structural information about the crystalline phases, characterizing the bulk region of the nanoparticle. XRPD does not provide information about the nanoparticle surface,[13] nor about the structure of small (< 1.5 nm) nanoparticles, which are too small to produce well-defined Bragg peaks.[21] For this reason, extended X-ray absorption fine structure (EXAFS)[22-24] is widely applied for nanostructured samples.[25-29] This technique yields averaged interatomic distances and coordination numbers around a specific atom type, does not require long range order, and is applicable to both crystalline and amorphous materials. As XRPD and EXAFS techniques are based on the scattering of photons and backscattering of photoelectrons, respectively, they are mostly sensitive to the heaviest atoms of the studied structure, being much less efficient (or almost inefficient) in detecting low Z atoms, such as carbon and hydrogen, present in metal carbides and hydrides. Unambiguous detection of hydride and carbide phases can be done by X-ray absorption near-edge structure (XANES) spectroscopy, which covers a short 30 - 50 eV range above the absorption edge.[30-40] As we have demonstrated in the previous works, XANES is able to distinguish Pd-H and Pd-C bonds via the difference in the structure of the unoccupied electronic states of palladium.[6, 12, 41]

Here, we report the formation of palladium hydrides and carbides in palladium NPs under reaction conditions of alkene and alkyne hydrogenation using *in situ* and *operando* and time-resolved synchrotron-based XRPD and X-ray absorption spectroscopy (XAS). By applying the simultaneous XRPD and EXAFS approach, we observed the formation of a core-shell structure in the palladium particles upon hydride phase formation during alkyne hydrogenation, characterized by different atomic structure of the inner "core" and surface "shell" regions. In the case of carbide formation, the additional introduction of XANES analysis to XRPD and EXAFS allowed observing the surface adsorbed carbon-containing molecules. In addition, we have developed a method which allows to estimate the H/Pd and C/Pd stoichiometries of PdH_x and PdC_y phases, by modelling and fitting the XANES spectra. Finally, application of operando time-resolved XRPD during the oscillatory reaction of ethylene to ethane conversion demonstrated, that not only the surface, but that also the core of the nanoparticles undergoes rapid structural changes, which correlate with the catalytic activity of the sample highlighting a direct structural-reactivity relationship.

2. Experimental and methods

2.1. Sample *preparation*

The catalyst investigated in this study has been supplied by Chimet S.p.A: product D1190 from the Chimet catalyst library (http://www.chimet.com/en/d1190). It is a 5 wt.% Pd on carbon catalyst prepared according to the deposition–precipitation method[42] on activated carbon of wood origin (surface area = 980 m^2g^{-1}; pore volume = 0.62 cm^3g^{-1}).[43, 44] Palladium black sample has been prepared following a procedure similar to that adopted for the catalyst preparation, but omitting the support, and successively reduced in H_2 at 120 °C, resulting in a stable bulk Pd^0 phase. TEM characterization of the catalyst resulted in a narrow particle size distribution with size *<D>* = 2.6 nm and σ = 0.4 nm, as detailed in a previous work.[13]

2.2. In situ *X-ray powder diffraction and X-ray absorption spectroscopy setup*

Both XRPD and Pd K-edge XAS data were collected at the BM01B[45, 46] (SNBL, now moved to the BM31 port) of the ESRF, Grenoble, France. The beamline allows a fast (less than 1 minute) plug and play switch between XRPD and XAS setups, allowing to measure for each reaction conditions (temperature and gas composition) both X-ray diffraction and absorption data.[12, 13, 47]

For *in situ* experiments, a boron glass capillary 1.0 mm in diameter filled with the catalyst powder and oriented horizontally and perpendicularly to the X-ray beam was used. A gas blower was positioned above the sample to define the temperature during the experiment. The capillary was glued into a metal holder connected with a pressurized setup, which allowed remotely controlling gas content (H_2 and/or C_2H_2) and pressure inside the capillary. The basal pressure, which was reached by using a scroll pump, was lower than 0.1 mbar. The surface Pd-oxide layer formed on the palladium NPs exposed to air,[48] was removed by performing a pretreatment at 125 °C in 200 mbar of pure H_2 for 30 minutes before data collection. For *operando* experiments, the 1.0-mm capillary was fed with the desired gas mixture (He, H_2 and/or C_2H_4) using calibrated gas flow-meters, while the composition of the gas outlet from the capillary was controlled by means of mass spectroscopy (MS) measured by a Pfeiffer Omnistar mass spectrometer (MS).

X-ray powder diffraction was measured using λ=0.50544(2) Å radiation, selected by a Si(111) channel-cut monochromator. CMOS-Dexela 2D detector positioned at the distance of 250.24(7) mm from the sample resulted in in a 2θ range from 5° to 52°, corresponding to a 5.79 to 0.57 Å d-spacing interval. The values of λ, sample to detector distance, and detectors tilts have been optimized by Rietveld refinement of NIST LaB_6 and Si samples and kept fixed in the refinement of the Pd/C samples. For better statistics 20 diffraction images and 20 dark images (with the X-ray shutter closed) with acquisition time of 1 s were collected in all cases. For the time resolved *operando* experiment, we were collecting 100 subsequent patterns with 5 second time-resolution, followed by 100 dark patterns.

XAS spectra at Pd K-edge were obtained in the transmission mode by continuous scanning of the double crystal Si(111) monochromator from 24100 to 25400 eV taking 5 minutes per spectrum. Pd foil was measured simultaneously with each spectrum for energy calibration using a third ionization chamber.[49] Detuning monochromathor crystals of 20% from the maximum intensity makes the contribution of the third harmonic at 75000 eV negligible.

2.3. Volumetric measurements

Hydrogen sorption isotherms were measured on a Micromeritics ASAP2020 volumetric apparatus. The instrument was equipped with 4 pressure transducers, allowing to investigate the sorption process at very low equilibrium pressures (down to 10^{-4} mbar). Prior to the measurements, the Pd/C powders (1.4 g) were activated on a vacuum line equipped with a turbomolecular pump (P < 10^{-4} mbar): after degassing at 120 °C for 3 h, the sample was subjected to two H_2 absorption/desorption cycles at 120 °C in hydrogen (absorption pressure: ~100 mbar, desorption pressure: dynamic vacuum) to guarantee a full reduction of the palladium nanoparticles. Then the sample was exposed to 100 mbar of H_2 and cooled down to room temperature. The sample was successively transferred inside a glove box (M Braun Lab Star Glove Box supplied with pure 5.5 grade N_2, < 0.5 ppm O_2, < 0.5 ppm H_2O) before being inserted into the measurement cell and degassed at room temperature for 1 h on the volumetric apparatus. The H_2 uptake of the bare carbon support was measured in the same conditions adopted for the Pd/C catalyst, after activation in dynamic vacuum at 120°C overnight. The isotherms reported in the following for the Pd/C systems were obtained from the measured ones after the subtraction of the H_2 uptake measured in the same conditions for the activated carbon support.

2.4. EXAFS, XANES and XRPD data analysis

X-ray absorption spectra were analyzed in Demeter 0.9.21 package[50] including background subtraction, normalization, energy calibration, and single-shell Fourier analysis. A real space data fitting in the R-range from 1.5 to 3.2 Å was performed to the Fourier-transformed k^2-weighted data in the k-range from 5.0 to 12.0 Å^{-1}, with the width of the window slope dk = 1 Å^{-1}, corresponding to the number of independent points $2\Delta k\Delta R/\pi > 7$. The low k-region ($2 - 5$ Å^{-1}) was intentionally excluded from the analysis to minimize the Pd-C contribution from interaction of the nanoparticles with the support. The fit included four parameters: the first shell Pd-Pd interatomic distance (R_{Pd-Pd}), the Debye-Waller factor (σ^2), energy shift (ΔE_0) and coordination number (N). The parameters ΔE_0 and N were considered as common variables for all spectra. The value of the passive electron reduction factor[51] $S_0^2 = 0.83 \pm 0.03$ was obtained by fitting the spectrum of palladium foil and kept constant in the optimization of all the spectra collected on the Pd-catalyst. Experimental spectra were fit in R-space using theoretical amplitudes and phases calculated by FEFF6 code.[52]

VASP 5.3 code[53-55] with PBE exchange-correlation potential,[56] was used to optimize the geometries of PdH$_x$ and PdC$_y$ phases. DFT-optimized PdH$_x$ and PdC$_y$ structures were then used for XANES calculation by FDMNES code.[36-40] Each spectrum, except pure metallic one, was calculated by averaging 32 separate theoretical spectra for each Pd atom in the optimized supercell. Calculation were performed within finite difference approach in full potential. 6 Å cluster around Pd absorbing atom was used in all simulations.

Fitting of experimental spectra by theoretical ones was performed by multidimensional interpolation method implemented in FitIt-3 code.[57, 58] Initially calculated spectra for given concentrations x, y in PdH$_x$, PdC$_y$ (x = 0, 0.125, 0.250, 0.500; y = 0, 0.063, 0.125, 0.250) were used as interpolation nodes to obtain spectra for all intermediate concentrations. To exclude systematic errors and increase precision, fitting was performed for difference XANES spectra. To plot the experimental difference spectra, we subtracted the spectrum of initial metallic palladium nanoparticles measured in

vacuum from all other spectra, while the theoretical ones were obtained after subtracting the fitted theoretical spectrum of metallic palladium nanoparticles.

2D XRPD patterns were processed by PyFAI[59] software which executes fast averaging, background subtraction and integration of images to obtain $I(2\theta)$ patterns. Rietveld refinement of static XRPD patterns was performed with Jana2006 code.[60] Profile parameters were optimized by fitting the diffraction patterns of bare and the most hydrogenated samples at each temperature. In the final refinement, we optimized of the fractions of α- and β- phases and the cell parameters corresponding to each phase. The time-resolved data was analysed by a linear combination fitting.

## 3. Results and discussion

3.1. Core-shell structures during hydride formation in palladium nanoparticles

Palladium hydride (PdH_x) may exist as two phases, named α and β, depending on the stoichiometric atomic ratio x.[61] For bulk palladium, the α-phase is present for values $0 < x \leq 0.03$, while the β-phase forms for values $x \geq 0.58$. Both phases are present for the intermediate values, which is often referred to as *plateau* in the hydrogen isotherm diagram. From a crystallographic point of view, PdH_x exhibits the same *fcc* space group as Pd metal with an increased lattice parameter (a), that shows stepwise behaviour at x values corresponding to the formation of α- and β- phases, while within each of the phases it linearly increases with x. The thermodynamics of hydrogen absorption of Pd NPs differs from the one of palladium bulk due to the considerable contribution of the surface.[9, 13, 62] The typical phase separation was observed in Pd NP down to nanometer size,[21, 63] but the relationship between hydrogen equilibrium pressure (EP) and H loading (x) differs significantly from bulk and strongly depends on the size and shape of the nanoparticles.[7] This affects both the maximum x value in the β-phase, and the extension the x-interval of coexistence of the two α- and β- phases in the plateau.

Figure 1 reports the XRPD and Pd K-edge XANES and EXAFS isotherms, respectively, collected at 22 °C, parts (a)-(c), respectively, of the PdH_x formation obtained by progressively increasing the H_2-EP from 0 to 1000 mbar. These X-ray absorption/diffraction experiments have been repeated for the isotherms at 1, 22, 53, 62 and 85 °C and duplicated with independent laboratory volumetric measurements (see Figure 2).

XRPD (Figure 2a) monitor the increase of the cell parameter a during the hydride formation, and is able to discriminate α and β phases, but it is scarcely informative for nanoparticles with size below 1 nm[21, 63] (that do not contribute to the Bragg reflections) and to the external shell of nanoparticles (because of disorder effects intrinsic of surface layers).[13] Being element specific,[22-24] EXAFS (Figure 2b) probes the local environment around the Pd absorbing atom, yielding average R_{Pd-Pd} values, coordination numbers and Debye-Waller parameters, and providing important complementary information on the surface of the nanoparticles,[13, 64-73] that is merged with the information on the core. Complementary volumetric measurements (Figure 2c) provide quantitative information on the x stoichiometry at given temperature and H_2-EP values, provided that the hydrogen uptake from the carbon support is properly taken into account.[13, 74, 75]
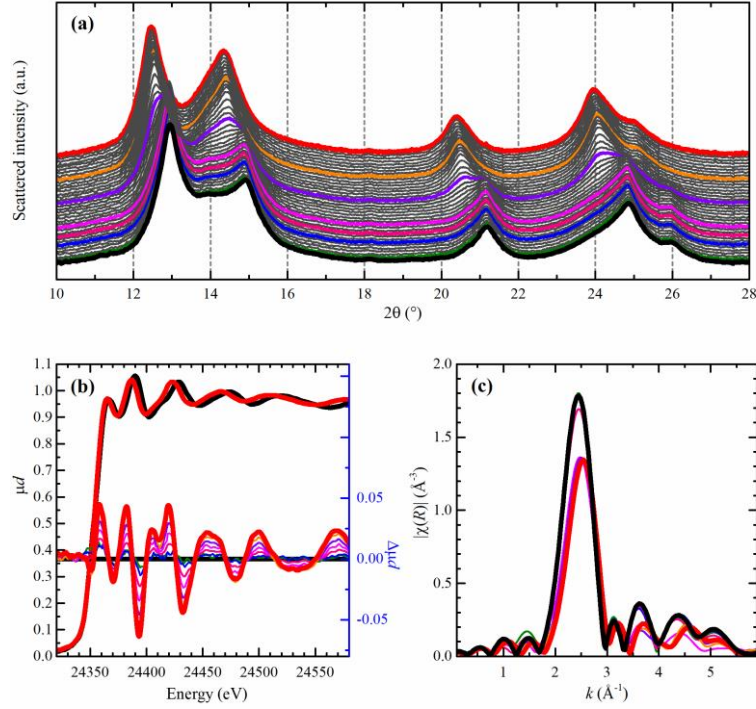
Figure 1. Evolution of the diffraction data and of the Pd K-edge X-ray absorption spectra along the Pd-hydride formation in Pd NPs at 22 °C obtained by increasing the H_2-EP in the pressure range from 0 (bold black) to 1000 (bold red) mbar range. Part (a): The whole series of the XRPD patterns where coloured intermediate patterns correspond to 1 (green), 10 (blue), 17 (pink), 20 (magenta), 25 (violet), 100 (orange). Part (b): XANES spectra obtained at H_2-EP of 0 (black curve) and 1000 mbar (red curve), left ordinate axis and ΔXANES spectra obtained by subtracting the spectrum of the metal phase, right ordinate axis. Part (c): Fourier-transformed k^2-wieghted $\chi(k)$ EXAFS functions. recorded under the same conditions. For sake of clarity only a fraction of the measured spectra is reported in parts (b-c), with the same colour code as for diffraction patterns reported in part (a). Previously unpublished figure reporting data published in Ref.[13]

Figure 2a,b reports the dependence of the cell parameter, a, and R_{Pd-Pd} value in the different points of the α/β phase diagrams of the PdH_x system as obtained from Rietveld refinement of XRPD and the first-shell analysis of the whole set of EXAFS data, respectively, collected at different H_2-EP during the five isotherms. At all investigated temperatures, the lattice expansion observed during the PdH_x phase formation is accompanied by an increase in the Debye-Waller parameter.[13] Being a phase-specific technique, XRPD is able to analyze separately the α- and β- hydride phases present in the sample at each point of the isotherm. The relative concentrations of the α- and β-phases and the cell parameters within each phase have been determined by a 2-phases Rietveld refinement procedure.[13] The structural isotherms obtained from XRPD has been plotted in Figure 2a in a way directly comparable with those obtained from the EXAFS analysis (Figure 2b) by reporting the averaged cell parameter as a weighted sum

$$a = (1-n) \cdot a_\alpha + n \cdot a_\beta, \tag{1}$$

where a_α and a_β are the refined lattice parameters of the α- and β- phases respectively, and n the refined fraction of the β-phase.

The Pd-specific pressure-composition isotherms for the Pd NPs, reported in Figure 2c, have been obtained by: (i) subtracting from the raw isotherms collected on the Pd/C samples the analogous isotherms collected on the bare carbon support and by (ii) correcting for the amount of hydrogen adsorbed at low pressure, which corresponds to

the formation of a hydrogen layer on the surface of the nanoparticles, and not to the formation of the hydride.[13] The nanometric dimensions of the Pd NPs resulted in a much lower hydrogen uptake of about $PdH_{0.4}$ in the β-phase region relative to $PdH_{0.6}$ reported for bulk palladium.[76-78] This observation reflects the lower number of interstitial sites per mass of palladium related to the higher surface to volume ratio[78] and the lower critical temperature[79-81] of Pd NPs with respect to the bulk.

The pressure-structure isotherms shown in Figure 2a,b are similar to the pressure-composition curves obtained from volumetric measurements (Figure 2c), which give information about the H/Pd ratio at any given temperature and pressure. All isotherms are characterized by three distinct regions: (i) the pre-plateau region, related to the formation of the α-phase (yellow region); (ii) the plateau, corresponding to the gradual phase transition from the solid solution to the β-phase (white region); (iii) the post-plateau region, where the solid solution of hydrogen in the metal hydride is formed (red region).[78] As widely reported for bulk palladium, the pressure corresponding to the plateau increases with the temperature and at the same time the miscibility gap of the solid solution with the hydride phase decreases.[61] As a consequence of the nanometric size, for Pd NPs the hydrogen-uptake and the lattice parameters at the end of each plateau are lower than that for bulk palladium at the same temperature.[13, 77, 78, 82] This effect is evident when comparing the structural and compositional isotherms obtained at 22 °C for Pd/C (blue scatters in Figure 2) and palladium black (dashed black line in Figure 2). However, the first shell EXAFS data themselves (Figure 2b) exhibit a less defined plateau than the corresponding XRPD data (Figure 2a). The plateau of the isotherms obtained by EXAFS are spanned in a wider pressure range with respect to the same plateau observed by XRPD at all the investigated temperatures. This discrepancy is absent for palladium black, indicating that it is a characteristic feature of the sample, and not a result of a different method.
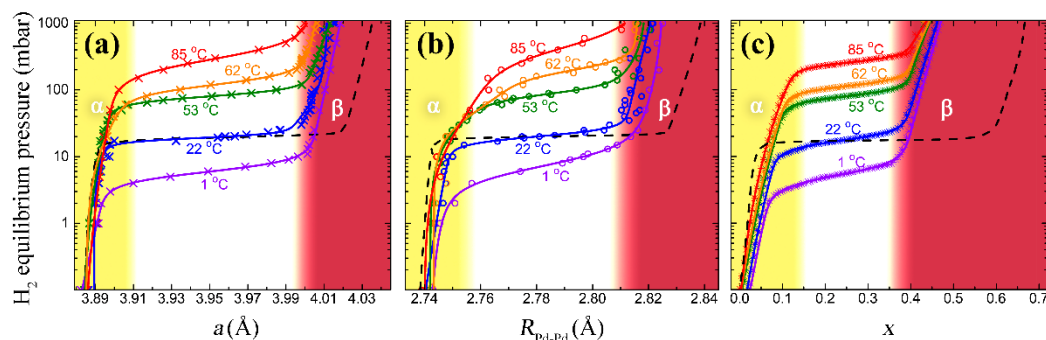

Figure 2. α/β phase diagrams of the PdH_x system evidenced in the pressure-R_{Pd-Pd}, pressure-a and pressure-x isotherms obtained from XRPD (a), EXAFS (b), and Pd-specific volumetry (c) for Pd/C at different temperatures (colored scatters) and palladium bulk (Pd-black) (black dashed line) at 22 °C. Solid colored lines correspond to the best fits by a model double-exponential function. The abscissa of part (a) is the averaged cell parameter defined in Eq. (1). Yellow, white and red regions define qualitatively pure α-, mixed-, and pure β- phases, respectively, for the Pd/C sample. Adapted with permission from Ref.[13], copyright ACS 2017.

The systematic difference in the behavior of the first shell EXAFS and XRPD data can be quantified by plotting the R_{Pd-Pd} value extracted from the XRPD isotherm ($R_{Pd-Pd} = a/\sqrt{2}$) together with the EXAFS isotherm, see Figure 3, green and black curves, respectively. This difference can be explained considering that the PdH_x NPs have a core-shell structure, with a crystalline core that contributes both to the Bragg reflections in the XRPD patterns and to the first shell Pd-Pd distance obtained by EXAFS, and an amorphous shell that contributes only to the latter observable.[13] This model is in line

with the evidence that the α-β phase separation does not exist and the pressure-composition isotherms lack the plateau region for Pd NPs with average size of 1 nm,[9] which do not give well-defined Bragg peaks.[21, 63] The theoretical Pd-Pd distance in the amorphous shell (R_{Pd-Pd}^{shell}) has been derived from the combined XRPD and EXAFS data, according to the following expression:[13]

$$C\ R_{Pd-Pd}^{shell} = R_{Pd-Pd}^{EXAFS} - (1 - C)\frac{1}{\sqrt{2}}\ a, \qquad (2)$$

where C is the fraction of atoms located in the amorphous shell. The red, blue and orange curves in Figure 3 reports the (R_{Pd-Pd}^{shell}) values obtained for the 22 °C isotherm assuming a C fraction of 0.5, 0.6 and 0.7, respectively. The shell absorbs hydrogen gradually, and the corresponding simulated isotherms result in a much less-defined α-β-phase transition.
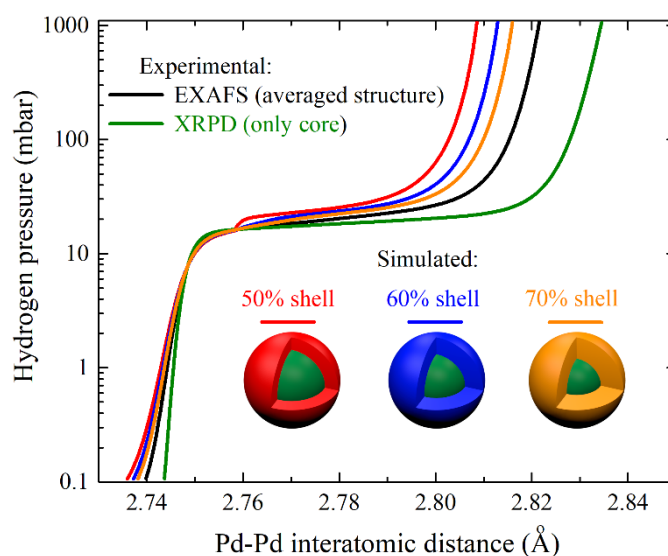

Figure 3. Simulated pressure-structure isotherm at 22 °C of hydride formation in the shell of the palladium particles assuming core/shell ratios of 50/50 (red), 40/60 (blue) and 30/70 (orange) derived from XRPD- (green) and EXAFS- (black) based experimental isotherms.

Summarizing, the synergic coupling of the three techniques highlights clear differences in the structural and electronic configuration of the palladium atoms in the shell and in the core of the nanoparticles during the Pd − PdH$_x$ phase transition.[13] The data reported in Figure 3 represent an important estimation of the R_{Pd-Pd} distance at the surface of the NP, i.e. the R_{Pd-Pd} of the actual active phase, where hydrogenation reactions occur.

3.2. Carbide formation in the core, in the shell and at the surface of Pd NPs

As shown in the previous section, both XRPD and EXAFS indicate formation of hydride phases by monitoring the increase of the interatomic distances that occurs due to the insertion of the hydrogen atoms into the palladium lattice. However, under reaction conditions, a palladium catalyst is exposed to a mixture of several gasses, such as H$_2$/C$_2$H$_4$, H$_2$/C$_2$H$_2$ or H$_2$/hydrocarnon, in general[2, 3] Under these conditions, formation of both palladium hydride and carbide phases is possible, which cannot be distinguished by standard EXAFS and XRPD analysis, as the lattice parameters for these phases are very similar, while amplitudes of photoelectron backscattering and photon scattering are much lower for H and C atoms than for Pd ones, not allowing their direct observation. However, direct observation of Pd-H and Pd-C bonds can be

done utilizing XANES spectra, which are sensitive to the presence of unoccupied states that result from mixing of Pd- and H- or C-orbitals.[12, 41] Figure 4a shows the typical Pd *K*-edge XANES spectra of palladium nanoparticles observed in vacuum conditions and after exposure of the sample to hydrogen and acetylene, to form hydride and carbide phases, respectively. The spectrum of PdH_x shows a sharpening of the first XANES peak and shifting to lower energies by about 1 eV, the opposite behavior is observed in the spectra after exposing the sample to acetylene and carbide formation. For better appreciation and further quantitative analysis, we have considered the difference XANES spectra, shown in Figure 4b, where the spectrum of Pd NPs in vacuum was subtracted from each of the other spectra. The typical features assigned to Pd-C bonds in the difference spectra are evolving with time, as shown by light red (15 minutes exposure to acetylene) and dark red (more than one hour exposure to acetylene) curves in Figure 4b. In addition, partially inversed behavior is observed when the catalyst is subsequently treated by H_2 and evacuated (Figure 4b, green curve).
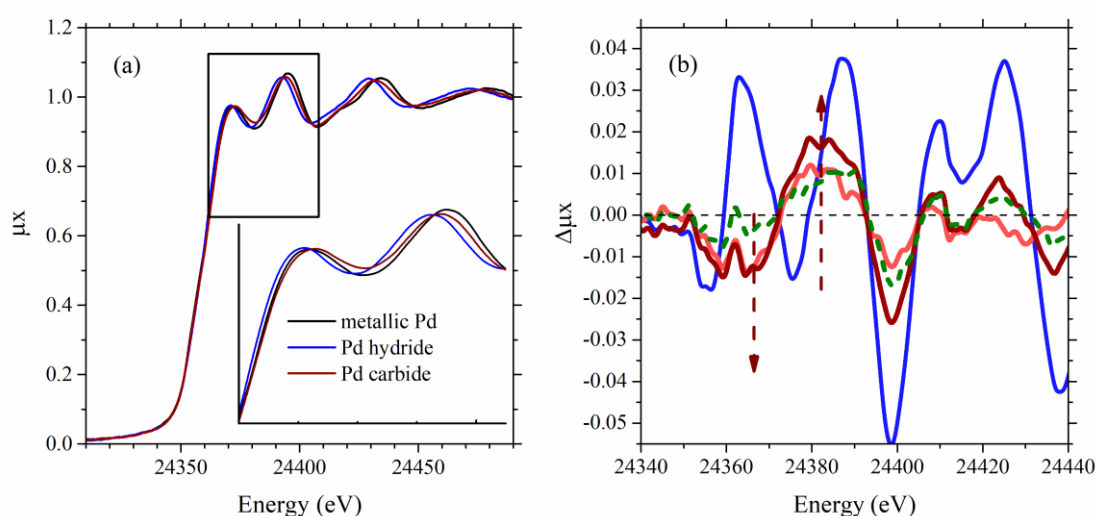

Figure 4. Part (a): experimental spectra of palladium nanoparticles in vacuum (black), in hydrogen (blue), and 1 hour of total exposure to acetylene (dark-red). Part (b) shows the corresponding difference XANES spectra with addition of the spectrum after 15 minutes exposure to acetylene (light-red) and after subsequent treatment in H_2 and successive outgassing (green). All the reported experiments have been performed with a sample temperature of 100 °C. See the orange triangles in Figure 5 for the quantitative results of the ΔXANES modelling and fitting procedure.

The time evolution of Pd NPs upon exposure to hydrogen, acetylene and vacuum conditions was studied by applying three independent approaches summarized in Figure 5. First, Rietveld refinement of XRPD patterns was performed to obtain the average cell parameter in the NPs, see grey circles in Figure 5, obtained applying Eq. (1). Second, the first-shell Fourier analysis of EXAFS spectra provided the averaged Pd-Pd interatomic distances (Figure 5, black squares). Finally, all experimental ΔXANES spectra were fitted (vide infra) by the theoretically calculated ones to obtain the concentration of carbon atoms per palladium atom, C/Pd, i.e. the *y* stoichiometry of the PdC_y phase (Figure 5, orange triangles).

In the 2:1 mixture of H_2 and C_2H_2 (green part in Figure 5), the averaged lattice parameter in the NPs is increased by ~ 3 %, with respect to pure palladium NPs, which is close to the values obtained in Section 3.1 for palladium hydride at 1000 mbar. In agreement with previous results,[12] the shape of ΔXANES spectra (Figure 4b, blue line) confirms that the hydride phase is formed under these conditions. In addition, a trial to

fit the ΔXANES spectra by theoretical signal for Pd-C resulted in the unphysical values of negative y values (Figure 5). The observed difference between the lattice expansion observed by EXAFS and XRPD correlates with the core-shell structure of the PdH$_x$ NPs (see Figure 3).

The removal of H$_2$ from the feed mixture (first light-red part in Figure 5), leads to a complete decomposition of the hydride phase, as al hydride features disappear from both XANES and ΔXANES spectra. However, the interatomic distances are higher by 0.5 % than in pure Pd NPs. This increase is explained by formation the palladium carbide phase, which is clearly observed in ΔXANES curves (Figure 4b) and formation of the second phase with increased lattice parameter visible in the XRPD patterns. There is a slow increase of the lattice parameter of the carbidized sample with continued C$_2$H$_2$ exposure time at 100 °C (light-red parts in Figure 5) and that it is not reversed neither by successive vacuum or treatment in H$_2$, see Figure 5 white and light-blue parts, respectively).
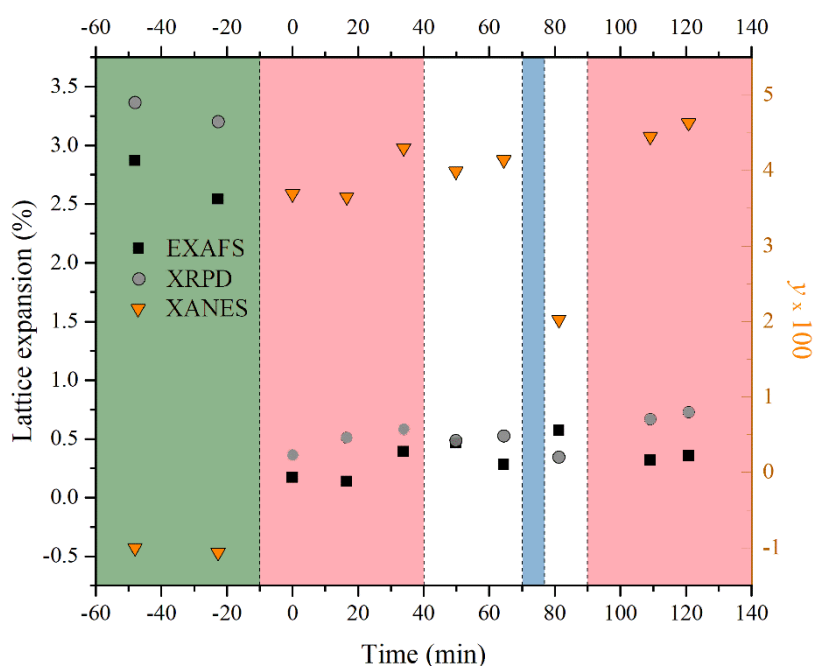
Figure 5. Evolution of structural parameters obtained from XRPD, EXAFS and ΔXANES analysis. Left ordinate axis: elongation of the $R_{Pd–Pd}$ distance (black squares) obtained from the first-shell EXAFS-analysis and of the variation of the average lattice parameter obtained from XRPD refinement (gray circles). Right ordinate axis: stoichiometry of the PdC$_y$ (in %) phase, determined by ΔXANES modelling and fitting (orange triangles). Exposure of the sample to pure H$_2$, C$_2$H$_2$ and vacuum are highlighted by light-blue, light-red and white areas respectively. In the region below t = 0, the sample was exposed to 1 bar of a mixture of hydrogen and acetylene in 2:1 stochiometric ratio (green area). All the reported experiments have been performed with a sample temperature of 100 °C.

To determine the evolution of the y stoichiometry in the PdC$_y$ carbide phase, all experimental ΔXANES spectra were fitted by the theoretical ones applying a multidimensional interpolation approach. A set of model structures with different y values and lattice parameters (thus different $R_{Pd-Pd} = a/\sqrt{2}$) were initially optimized with help of the VASP 5.3 code[53-55] and used for XANES calculation with the FDMNES code,[36-40] as described in Section 2.3. The calculated spectra were then taken as interpolation nodes in the two-dimensional (R_{Pd-Pd}, y) space, and used for construction of a polynomial which describes the shape of the ΔXANES spectra for any of the R_{Pd-}

Pd and *y* values. At the first step, we fitted the experimental XANES spectrum of Pd NPs in vacuum, and used the best fit theoretical spectrum to construct theoretical ΔXANES curves. All other spectra were fitted by minimizing the root-mean-square deviation $F(R_{Pd\text{-}Pd}, y)$ between theoretical and experimental ΔXANES spectra, varying $R_{Pd\text{-}Pd}$ and y values defined as:

$$F(R_{Pd-Pd}, y) = \frac{1}{Norm}\sqrt{\sum_{i=1}^{N}[\Delta XANES^{exp}(E_i) - \Delta XANES^{theo}(E_i, R_{Pd-Pd}, y)]^2} \quad (3)$$

where E_i are the energy values where the experimental curves have been sampled, $E_1 = 24340$ eV and $E_N = 24440$ eV are the first and the last experimental points considered in the fit and N is the total number of experimental points. The 2D distributions of $F(R_{Pd\text{-}Pd}, y)$ for selected spectra are shown in Figure 6. For the spectrum taken in H_2 ($t = -22$ min), the minimum of F is achieved for the increased $R_{Pd\text{-}Pd}$ and indicates zero carbon incorporation (y = −0.01, i.e. y = 0 within the experimental incertitude). This result represents a consistence test of the adopted method. An increase of the carbon incorporation is observed after acetylene exposure and the position of the minimum of F shifts towards higher y values from the spectrum taken at $t = 0$, to $t = 120$ min, where the time corresponds the starting time of each spectrum. The only deviation from the increasing y trend is observed after H_2 treatment of the sample ($t = 81$ min), which leads to decrease of *y* by a factor of 2. This difference is observed only in the XANES spectra, while the EXAFS and XRPD values are not affected by H_2 treatment. The reason of such behavior is that XANES spectra are sensitive not only to carbon atoms which are inserted in the interstitials of the palladium lattice forming palladium carbide phase, but also the surface adsorbed acetylene molecules, which do not affect the interatomic distance but contribute to the number of Pd-C bonds. H_2 treatment can be therefore used to remove the surface acetylene by its hydrogenation to ethylene and ethane, while it does not remove the carbon atoms from the palladium lattice.[15] This unambiguously shows that the use of XANES spectra, in addition to EXAFS and XRPD, allows to extract information on the structure of surface atoms, in addition to the core-shell structure which is revealed by combination the latter two.[13]

In this case XANES was used as a completely independent technique that provides both structure ($R_{Pd\text{-}Pd}$), and stoichiometry (y) of the PdC_y phase. However, given that Fourier-analysis of the EXAFS data has been performed, the $R_{Pd\text{-}Pd}$ values can be fixed to those obtained by EXAFS analysis. For the current data set, as can be seen from Figure 6, $F(R_{Pd\text{-}Pd}, y)$ functions are symmetric with respect to horizontal and vertical dashed lines passing through the minimal point of each spectrum. Thus, for this particular case, having an error in determination of $R_{Pd\text{-}Pd}$ value does not affect the position of the minimum along the *y* axis, while in case of an asymmetric distribution of the F function, the use of EXAFS interatomic distances would have been more critical.
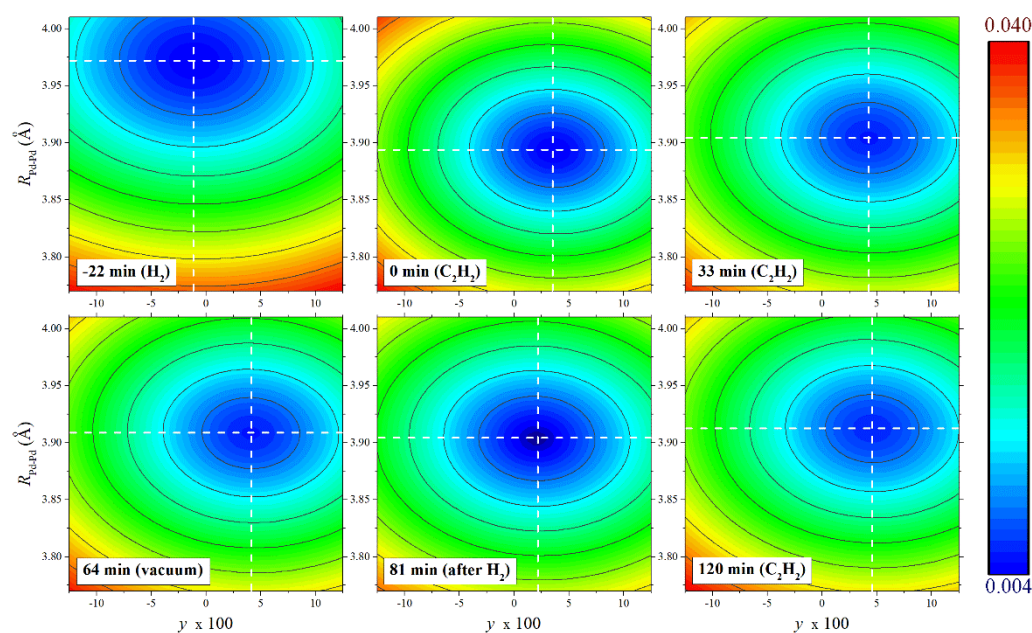
Figure 6. 2D plots of the $F(R_{Pd-Pd}, y)$ root-mean-square deviation function between theoretical and experimental ΔXANES spectra, defined in Eq. (3) for different experimental curves collected at time indicated in the bottom left corner and referred to the feeding conditions defined in Figure 5. The white dotted lines highlight the position of the minimum for each spectrum corresponding to the best estimation for R_{Pd-Pd} and y values of the PdC_y phase in the corresponding experimental conditions. The used color scale is quantified in the right panel. The fact that there is one order of magnitude in the intensity differences between blue and red regions implies that in all cases we are dealing with quite stable minima.

3.3. *Operando* hydrogenation of ethylene: evidence of structural and catalytic oscillation behavior

XRPD patterns were collected every 5 s under steady state gas feeding of the Pd/C catalyst (6, 39 and 5 ml/min for He, H_2 and C_2H_4, respectively) allowing to monitor the structural parameters of the core of the Pd NP during ethylene hydrogenation at 80 °C. The results of this *operando* XRPD study are summarized in Figure 7. Part (a) reports the 2θ region covering the (220), (311) and (222) Bragg reflections of palladium for a series of 10 subsequent diffractograms (from $t = 100$ to $t = 150$ s). Form these data it is evident, that during a steady state feeding conditions the structure of the core of the Pd NPs is not stable, but changes in time. Figure 7b, left ordinate axis, reports the time evolution of the average lattice parameter, obtained using Eq. (1). From these data, it is evident that the structural changes are not random but follow a clear oscillation behavior with a period of about 150 s. The periodic lattice parameter variation is due to the periodic variation of the relative fraction of the β- and α-phases of palladium hydride (see section 3.1 in general and Figure 2b in particular) and here reported in Figure 7b, right ordinate axis. The most interesting aspect of this experiment is the fact that the same periodic oscillations of non-regular shape were observed by MS monitoring for both reactants and products, see Figure 7c. Indeed, the MS signal of the C_2H_6 product ($m/Z = 30$) is in perfect phase with the oscillation of the fraction of β-phase of PdH obtained by XRPD, while the MS signal of the H_2 reactant ($m/Z = 2$) is in perfect antiphase.

These evidences are a direct unconfutable proof of a strong structure-reactivity relationship between the structure of the core of the PdH_x NPs and the catalyst activity in the ethylene hydrogenation reaction. Also evident is the fact that the catalyst is more

active in the $H_2 + C_2H_4 \rightarrow C_2H_6$ reaction when the core of the PdH_x NPs is in the β-phase, in agreement with previous findings.[14] Not straightforward is however the interpretation of observed oscillatory behavior on an atomistic point of view. Two, non-mutually exclusive, hypotheses are able to explain the set of experimental data summarized in Figure 7.
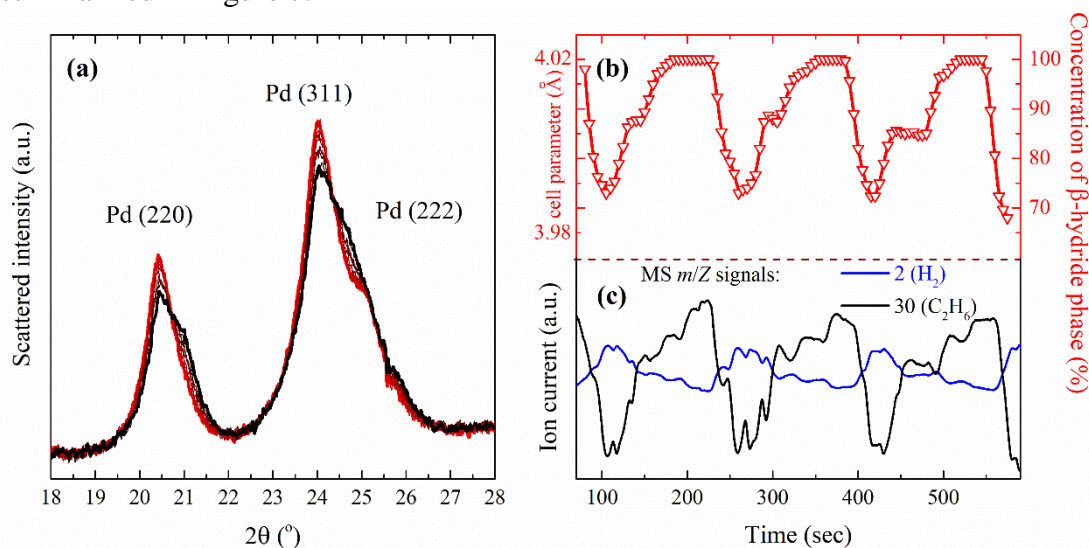
Figure 7. Time resolved, *operando* XRPD study during ethylene hydrogenation reaction at 80 °C on Pd/C catalyst performed under steady state feeding conditions: (6, 39 and 5 ml/min for He, H_2 and C_2H_4, respectively). Part (a): selection of XRPD patterns at significant times (from $t = 100$ to $t = 150$ s), evidencing structural changes along the reaction monitored in the 2θ range of the most significant Pd Bragg reflections. Part (b): time evolution of the averaged Pd lattice parameter, see Eq. (1), and of the fraction of β-phase of PdH_x left and right ordinate axis, respectively. Part (c): time evolution of the catalyst activity monitored by MS showing a reactant (H_2, $m/Z = 2$) and a product (C_2H_6, $m/Z = 30$).

Starting from with the core of the PdH_x NPs fully in the β-phase (e.g. at t = 200 s in Figure 7), we have a fully active catalyst. Owing to the exothermicity of the ethylene hydrogenation reaction ($\Delta H^0 = -136$ kJ/mol),[83, 84] the NPs undergoes a local temperature increase, that results in a partial hydrogen desorption (see Figure 2), that in turns results in a decrease of the fraction of the β-phase. At this stage, the catalyst undergoes a loss of activity, that in the successive seconds drives a local temperature decrease and an increase of the average H_2 partial pressure in the feed, that favors additional hydrogen uptake, with the progressive restoration of the fully β-phase and higher catalytic activity.

Alternatively, we can consider the fact that the ethylene hydrogenation at the surface of the NPs requires atomic hydrogen from the bulk. Let us start again our arguments at $t = 200$ s in Figure 7, when we have a highly active catalyst with the core of the PdH_x NPs fully in the β-phase. The high surface activity requires an important transport of hydrogen atoms from the core, with the consequent x depletion and the decrease of β-phase fraction. The increase of the relative fraction of the less active α-phase in the NP core causes a decrease of the catalyst activity with consequent increase of the H_2 partial pressure in the atmosphere. The additional H_2 available is then absorbed back by the NPs, progressively restoring β-hydride phase with consequent increase of the reaction rate.

4. Conclusions and future perspectives

In the present study, we have combined synchrotron-based *in situ* and *operando*, almost simultaneous, X-ray diffraction and absorption data collection to laboratory volumetric measurements to shed light on the structure and the stoichiometry of PdH_x and PdC_y phases of Pd NPs during hydrocarbons hydrogenation reactions on Pd/C catalyst. Six main results have been achieved.

First, the systematic *in situ* XRPD, EXAFS and volumetric analysis in a wide range of sample temperatures and H_2 equilibrium pressures, allowed us to follow the $\alpha-\beta$ phase transition diagram. The structural/stoichiometric the $\alpha-\beta$ phase diagram reported in Figure 2a,b,c allowed us to determine the PdH_x stoichiometry form an EXAFS or an XRPD structural datum. Second, the almost simultaneous EXAFS and XRPD set of data allowed us to discriminate the ordered NP core from the disordered shell and to reconstruct the R_{Pd-Pd} distance at the surface of the NP, i.e. the the R_{Pd-Pd} of the actual active phase, where hydrogenation reactions occur (Figure 3). Third, while both XRPD and EXAFS are unable to discriminate between palladium hydride and carbide phases, XANES provides unambiguous detection of hydride and carbide phases (Figure 4a), being the discrimination ability more evident when the data are reported in difference mode (ΔXANES, Figure 4b). Fourth, the combined use of XRPD, EXAFS and XANES, supported by corresponding simulations, allowed us to obtain both core and shell structure and average *y* stoichiometry of the PdC_y phase obtained exposure of Pd NPs to C_2H_2 at increasing times (Figure 5 and Figure 6). Fifth, advanced analysis of the ΔXANES spectra allows detection of carbon-containing molecules adsorbed at surface of the NPs. Finally, the collection of *operando* XRPD patterns allowed us to highlight during ethylene hydrogenation reaction periodic oscillations of non-regular shape of the NPs core lattice parameter, that resulted to be in phase with the MS signal of the C_2H_6 product and in antiphase with the MS signal of the H_2 (Figure 7), highlighting an interesting direct structural-reactivity relationship. Two, non-mutually exclusive, hypothesis have been put forward to explain the combined structural-reactivity study from an atomistic point of view.

A repetition rate of 0.2 Hz (one XRPD pattern every 5 s) was needed to follow the structural oscillation of the core. Unfortunately, 5 s were insufficient to obtain an EXAFS spectrum in quick EXAFS mode[85] with a sufficient signal to noise (on our Pd/C sample hosted in a capillary) to allow an accurate determination of the structure of the shell. This experiment should be repeated using an EXAFS dispersive beamline.[86]

Acknowledgments

Notes and references

1.   A. Molnar, A. Sarkany and M. Varga, *J. Mol. Catal. A-Chem.*, 2001, **173**, 185-221.
2.   A. Borodzinki, *Catal. Rev.-Sci. Eng.*, 2006, **48**, 91-144.

3. A. Borodzinski and G. C. Bond, *Catal. Rev.-Sci. Eng.*, 2008, **50**, 379-469.
4. M. Armbruster, M. Behrens, F. Cinquini, K. Fottinger, Y. Grin, A. Haghofer, B. Klotzer, A. Knop-Gericke, H. Lorenz, A. Ota, S. Penner, J. Prinz, C. Rameshan, Z. Revay, D. Rosenthal, N. Rupprechter, P. Sautet, R. Schlogl, L. D. Shao, L. Szentmiklosi, D. Teschner, D. Torres, R. Wagner, R. Widmer and G. Wowsnick, *ChemCatChem*, 2012, **4**, 1048-1063.
5. J. A. McCaulley, *J. Phys. Chem.*, 1993, **97**, 10372-10379.
6. A. V. Soldatov, S. Dellalonga and A. Bianconi, *Solid State Commun.*, 1993, **85**, 863-868.
7. S. Kishore, J. A. Nelson, J. H. Adair and P. C. Eklund, *J. Alloy. Compd.*, 2005, **389**, 234-242.
8. M. Yamauchi, R. Ikeda, H. Kitagawa and M. Takata, *J. Phys. Chem. C*, 2008, **112**, 3294-3299.
9. C. Langhammer, E. M. Larsson, B. Kasemo and I. Zoric, *Nano Lett.*, 2010, **10**, 3529-3538.
10. T. Shegai and C. Langhammer, *Adv. Mater.*, 2011, **23**, 4409-+.
11. A. L. Bugaev, A. A. Guda, K. A. Lomachenko, V. V. Srabionyan, L. A. Bugaev, A. V. Soldatov, C. Lamberti, V. P. Dmitriev and J. A. van Bokhoven, *J. Phys. Chem. C*, 2014, **118**, 10416-10423.
12. A. L. Bugaev, A. A. Guda, A. Lazzarini, K. A. Lomachenko, E. Groppo, R. Pellegrini, A. Piovano, H. Emerich, A. V. Soldatov, L. A. Bugaev, V. P. Dmitriev, J. A. van Bokhoven and C. Lamberti, *Catal. Today*, 2017, **283**, 119-126.
13. A. L. Bugaev, A. A. Guda, K. A. Lomachenko, V. V. Shapovalov, A. Lazzarini, J. G. Vitillo, L. A. Bugaev, E. Groppo, R. Pellegrini, A. V. Soldatov, J. A. van Bokhoven and C. Lamberti, *J. Phys. Chem. C*, 2017, **121**, 18202-18213.
14. D. Teschner, J. Borsodi, A. Wootsch, Z. Revay, M. Havecker, A. Knop-Gericke, S. D. Jackson and R. Schlogl, *Science*, 2008, **320**, 86-89.
15. M. W. Tew, M. Nachtegaal, M. Janousch, T. Huthwelker and J. A. van Bokhoven, *Phys. Chem. Chem. Phys.*, 2012, **14**, 5761-5768.
16. D. Teschner, Z. Revay, J. Borsodi, M. Havecker, A. Knop-Gericke, R. Schlogl, D. Milroy, S. D. Jackson, D. Torres and P. Sautet, *Angew. Chem.-Int. Edit.*, 2008, **47**, 9274-9278.
17. D. Teschner, J. Borsodi, Z. Kis, L. Szentmiklosi, Z. Revay, A. Knop-Gericke, R. Schlogl, D. Torres and P. Sautet, *J. Phys. Chem. C*, 2010, **114**, 2293-2299.
18. M. W. Tew, M. Janousch, T. Huthwelker and J. A. van Bokhoven, *J. Catal.*, 2011, **283**, 45-54.
19. W. Vogel, W. He, Q. H. Huang, Z. Q. Zou, X. G. Zhang and H. Yang, *Int. J. Hydrog. Energy*, 2010, **35**, 8609-8620.
20. Z. A. Chase, J. L. Fulton, D. M. Camaioni, D. H. Mei, M. Balasubramanian, V. T. Pham, C. Zhao, R. S. Weber, Y. Wang and J. A. Lercher, *J. Phys. Chem. C*, 2013, **117**, 17603-17612.
21. D. G. Narehood, S. Kishore, H. Goto, J. H. Adair, J. A. Nelson, H. R. Gutierrez and P. C. Eklund, *Int. J. Hydrog. Energy*, 2009, **34**, 952-960.
22. A. Filipponi, A. DiCicco and C. R. Natoli, *Phys. Rev. B*, 1995, **52**, 15122-15134.
23. J. J. Rehr and R. C. Albers, *Rev. Mod. Phys.*, 2000, **72**, 621-654.
24. J. A. van Bokhoven and C. Lamberti, *X-Ray Absorption and X-Ray Emission Spectroscopy: Theory and Applications*, John Wiley & Sons, Chichester (UK), 2016.
25. C. Lamberti, *Surf. Sci. Rep.*, 2004, **53**, 1-197.

26. S. Bordiga, E. Groppo, G. Agostini, J. A. van Bokhoven and C. Lamberti, *Chem. Rev.*, 2013, **113**, 1736-1850.

27. L. Mino, G. Agostini, E. Borfecchia, D. Gianolio, A. Piovano, E. Gallo and C. Lamberti, *J. Phys. D-Appl. Phys.*, 2013, **46**, 72.

28. C. Garino, E. Borfecchia, R. Gobetto, J. A. van Bokhoven and C. Lamberti, *Coord. Chem. Rev.*, 2014, **277**, 130-186.

29. C. Lamberti and J. A. van Bokhoven, in *X-Ray Absorption and X-Ray Emission Spectroscopy: Theory and Applications*, eds. J. A. van Bokhoven and C. Lamberti, John Wiley & Sons, Chichester (UK), 2016, vol. II, ch. 13, pp. 353-383.

30. A. Bianconi, J. Garcia and M. Benfatto, *Top. Curr. Chem.*, 1988, **145**, 29-67.

31. M. Benfatto and S. Della Longa, *J. Synchrotron Radiat.*, 2001, **8**, 1087-1094.

32. M. Benfatto, S. Della Longa and C. R. Natoli, *J. Synchrotron Radiat.*, 2003, **10**, 51-57.

33. C. R. Natoli, M. Benfatto, S. Della Longa and K. Hatada, *J. Synchrotron Radiat.*, 2003, **10**, 26-42.

34. A. L. Ankudinov, B. Ravel, J. J. Rehr and S. D. Conradson, *Phys. Rev. B*, 1998, **58**, 7565-7576.

35. J. J. Rehr and A. L. Ankudinov, *Coord. Chem. Rev.*, 2005, **249**, 131-140.

36. Y. Joly, *Phys. Rev. B*, 2001, **63**, 10.

37. O. Bunau and Y. Joly, *J. Phys.-Condes. Matter*, 2009, **21**, 11.

38. Y. Joly and S. Grenier, in *X-Ray Absorption and X-Ray Emission Spectroscopy: Theory and Applications*, eds. J. A. van Bokhoven and C. Lamberti, John Wiley & Sons, Chichester (UK), 2016, vol. I, ch. 4, pp. 73-97.

39. S. A. Guda, A. A. Guda, M. A. Soldatov, K. A. Lomachenko, A. L. Bugaev, C. Lamberti, W. Gawelda, C. Bressler, G. Smolentsev, A. V. Soldatov and Y. Joly, *J. Chem. Theory Comput.*, 2015, **11**, 4512-4521.

40. A. A. Guda, S. A. Guda, M. A. Soldatov, K. A. Lomachenko, A. L. Bugaev, C. Lamberti, W. Gawelda, C. Bressler, G. Smolentsev, A. V. Soldatov and Y. Joly, *J. Phys.: Conf. Ser.*, 2016, **712**, Art. n. 012004.

41. A. L. Bugaev, V. V. Srabionyan, A. V. Soldatov, L. A. Bugaev and J. A. van Bokhoven, *J. Phys. Conf. Ser.*, 2013, **430**, Art. n. 012028.

42. G. Poncelet, P. Jacobs and P. Grange, *Preparation of catalysts III*, Elsevier, 1983.

43. G. Agostini, C. Lamberti, R. Pellegrini, G. Leofanti, F. Giannici, A. Longo and E. Groppo, *ACS Catal.*, 2014, **4**, 187-194.

44. A. Piovano, A. Lazzarini, R. Pellegrini, G. Leofanti, G. Agostini, S. Rudić, A. L. Bugaev, C. Lamberti and E. Groppo, *Adv. Condens. Matter Phys.*, 2015, **2015**, Art. n. 803267.

45. W. van Beek, O. V. Safonova, G. Wiker and H. Emerich, *Phase Transit.*, 2011, **84**, 726-732.

46. P. M. Abdala, O. V. Safonova, G. Wiker, W. van Beek, H. Emerich, J. A. van Bokhoven, J. Sa, J. Szlachetko and M. Nachtegaal, *Chimia*, 2012, **66**, 699-705.

47. C. W. Andersen, E. Borfecchia, M. Bremholm, M. R. V. Jorgensen, P. N. R. Vennestrom, C. Lamberti, L. F. Lundegaard and B. B. Iversen, *Angew. Chem.-Int. Edit.*, 2017, **56**, 10367-10372.

48. E. Groppo, G. Agostini, A. Piovano, N. B. Muddada, G. Leofanti, R. Pellegrini, G. Portale, A. Longo and C. Lamberti, *J. Catal.*, 2012, **287**, 44-54.

49. C. Lamberti, S. Bordiga, F. Bonino, C. Prestipino, G. Berlier, L. Capello, F. D'Acapito, F. Xamena and A. Zecchina, *Phys. Chem. Chem. Phys.*, 2003, **5**, 4502-4509.
50. B. Ravel and M. Newville, *J. Synchrotron Radiat.*, 2005, **12**, 537-541.
51. J. J. Kas, A. P. Sorini, M. P. Prange, L. W. Cambell, J. A. Soininen and J. J. Rehr, *Phys. Rev. B*, 2007, **76**, 10.
52. S. I. Zabinsky, J. J. Rehr, A. Ankudinov, R. C. Albers and M. J. Eller, *Phys. Rev. B*, 1995, **52**, 2995-3009.
53. G. Kresse and J. Furthmuller, *Phys. Rev. B*, 1996, **54**, 11169-11186.
54. G. Kresse and D. Joubert, *Phys. Rev. B*, 1999, **59**, 1758-1775.
55. J. Hafner, *J. Comput. Chem.*, 2008, **29**, 2044-2078.
56. J. P. Perdew, K. Burke and M. Ernzerhof, *Phys. Rev. Lett.*, 1996, **77**, 3865-3868.
57. G. Smolentsev and A. Soldatov, *J. Synchrotron Radiat.*, 2005, **13**, 19-29.
58. G. Smolentsev and A. V. Soldatov, *Comp. Mater. Sci.*, 2007, **39**, 569-574.
59. J. Kieffer and J. P. Wright, *Powder Diffract.*, 2013, **28**, S339-S350.
60. V. Petříček, M. Dušek and L. Palatinus, *Z. Kristallog.*, 2014, **229**, 345-352.
61. F. A. Lewis, *Platin. Met. Rev.*, 1982, **26**, 70-78.
62. C. Langhammer, V. P. Zhdanov, I. Zoric and B. Kasemo, *Chem. Phys. Lett.*, 2010, **488**, 62-66.
63. B. Ingham, M. F. Toney, S. C. Hendy, T. Cox, D. D. Fong, J. A. Eastman, P. H. Fuoss, K. J. Stevens, A. Lassesson and S. Brown, *Phys. Rev. B*, 2008, **78**, Art. n. 245408.
64. G. L. Chiarello and D. Ferri, *Phys. Chem. Chem. Phys.*, 2015, **17**, 10579-10591.
65. D. Ferri, M. S. Kumar, R. Wirz, A. Eyssler, O. Korsak, P. Hug, A. Weidenkaff and M. A. Newton, *Phys. Chem. Chem. Phys.*, 2010, **12**, 5634-5646.
66. D. Ferri, M. A. Newton, M. Di Michiel, G. L. Chiarello, S. Yoon, Y. Lu and J. Andrieux, *Angew. Chem.-Int. Edit.*, 2014, **53**, 8890-8894.
67. A. I. Frenkel, C. W. Hills and R. G. Nuzzo, *J. Phys. Chem. B*, 2001, **105**, 12689-12703.
68. A. I. Frenkel, A. Yevick, C. Cooper and R. Vasic, *Ann. Rev. Anal. Chem.*, 2011, **4**, 23-39.
69. A. I. Frenkel, *Chem. Soc. Rev.*, 2012, **41**, 8163-8178.
70. G. Agostini, R. Pellegrini, G. Leofanti, L. Bertinetti, S. Bertarione, E. Groppo, A. Zecchina and C. Lamberti, *J. Phys. Chem. C*, 2009, **113**, 10485-10492.
71. G. Agostini, E. Groppo, A. Piovano, R. Pellegrini, G. Leofanti and C. Lamberti, *Langmuir*, 2010, **26**, 11204-11211.
72. G. Agostini, A. Piovano, L. Bertinetti, R. Pellegrini, G. Leofanti, E. Groppo and C. Lamberti, *J. Phys. Chem. C*, 2014, **118**, 4085-4094.
73. M. Manzoli, F. Vindigni, T. Tabakova, C. Lamberti, D. Dimitrov, K. Ivanov and G. Agostini, *J. Mater. Chem. A*, 2017, **5**, 2083-2094.
74. A. L. Bugaev, A. A. Guda, K. A. Lomachenko, A. Lazzarini, V. V. Srabionyan, J. G. Vitillo, A. Piovano, E. Groppo, L. A. Bugaev, A. V. Soldatov, V. P. Dmitriev, R. Pellegrini, J. A. van Bokhoven and C. Lamberti, *J. Phys. Conf. Ser.*, 2016, **712**, Art. n. 012032.
75. R. Campesi, F. Cuevas, R. Gadiou, E. Leroy, M. Hirscher, C. Vix-Guterl and M. Latroche, *Carbon*, 2008, **46**, 206-214.
76. T. B. Flanagan and W. A. Oates, *Annu. Rev. Mater. Sci.*, 1991, **21**, 269-304.
77. R. Griessen, N. Strohfeldt and H. Giessen, *Nat. Mater.*, 2016, **15**, 311-317.
78. A. Zuttel, C. Nutzenadel, G. Schmid, C. Emmenegger, P. Sudan and L. Schlapbach, *Appl. Surf. Sci.*, 2000, **162**, 571-575.

79. A. Baldi, T. C. Narayan, A. L. Koh and J. A. Dionne, *Nat. Mater.*, 2014, **13**, 1143-1148.
80. R. Bardhan, L. O. Hedges, C. L. Pint, A. Javey, S. Whitelam and J. J. Urban, *Nat. Mater.*, 2013, **12**, 905-912.
81. S. Syrenova, C. Wadell, F. A. A. Nugroho, T. A. Gschneidtner, Y. A. D. Fernandez, G. Nalin, D. Switlik, F. Westerlund, T. J. Antosiewicz, V. P. Zhdanov, K. Moth-Poulsen and C. Langhammer, *Nat. Mater.*, 2015, **14**, 1236-1244.
82. C. Zlotea, F. Cuevas, V. Paul-Boncour, E. Leroy, P. Dibandjo, R. Gadiou, C. Vix-Guterl and M. Latroche, *J. Am. Chem. Soc.*, 2010, **132**, 7720-7729.
83. G. B. Kistiakowsky and A. G. Nickle, *Discussions of the Faraday Society*, 1951, **10**, 175-187.
84. G. B. Kistiakowsky, H. Romeyn, J. R. Ruhoff, H. A. Smith and W. E. Vaughan, *J. Am. Chem. Soc.*, 1935, **57**, 65-75.
85. M. Nachtegaal, O. Müller, C. König and R. Frahm, in *X-Ray Absorption and X-Ray Emission Spectroscopy: Theory and Applications*, eds. J. A. van Bokhoven and C. Lamberti, John Wiley & Sons, Chichester (UK), 2016, vol. I, ch. 7, pp. 155-183.
86. Mathon Olivier, I. Kantor and S. Pascarelli, in *X-Ray Absorption and X-Ray Emission Spectroscopy: Theory and Applications*, eds. J. A. van Bokhoven and C. Lamberti, John Wiley & Sons, Chichester (UK), 2016, vol. I, ch. 8, pp. 185-212.